APL Materials

RESEARCH ARTICLE | AUGUST 13 2025

Characterization of extended defect evolution in 1.2–12 μm thick homoepitaxial (010) β-Ga_2O_3 grown by close-injection showerhead metal-organic chemical vapor deposition

Special Collection: Ultrawide Bandgap Semiconductors

Marko J. Tadjer ; Kenny Hyunh ; James C. Culbertson ; Evan R. Glaser ; Michael E. Liao ; John Gaskins ; Hannah N. Masten ; Alan G. Jacobs ; Nadeem A. Mahadik ; James Spencer Lundh ; Jaime A. Freitas,, Jr. ; Fikadu Alema ; Andrei Osinsky ; Patrick Hopkins ; Mark Goorsky ; Karl D. Hobart

APL Mater. 13, 081117 (2025)
https://doi.org/10.1063/5.0268313
CHORUS

Characterization of extended defect evolution in 1.2–12 μm thick homoepitaxial (010) β-Ga_2O_3 grown by close-injection showerhead metal-organic chemical vapor deposition

Cite as: APL Mater. 13, 081117 (2025); doi: 10.1063/5.0268313
Submitted: 28 February 2025 • Accepted: 14 July 2025 •
Published Online: 13 August 2025

Marko J. Tadjer,[1,a)] Kenny Hyunh,[2] James C. Culbertson,[1] Evan R. Glaser,[1] Michael E. Liao,[2,3] John Gaskins,[4] Hannah N. Masten,[3] Alan G. Jacobs,[1] Nadeem A. Mahadik,[1] James Spencer Lundh,[1] Jaime A. Freitas, Jr.,[1] Fikadu Alema,[5] Andrei Osinsky,[5] Patrick Hopkins,[4,6] Mark Goorsky,[2] and Karl D. Hobart[1]

AFFILIATIONS

[1] U.S. Naval Research Laboratory, Washington, District of Columbia 20375, USA
[2] University of California, Los Angeles, California 90095, USA
[3] National Research Council Postdoctoral Fellow, Washington, District of Columbia 20375, USA
[4] LaserThermal Inc., Charlottesville, Virginia 22902, USA
[5] Agnitron Technology, Chanhassen, Minnesota 55317, USA
[6] University of Virginia, Charlottesville, Virginia 22903, USA

Note: This paper is part of the Special Topic on Ultra-wide Bandgap Semiconductors.
[a)] **Author to whom correspondence should be addressed:** marko.tadjer@nrl.navy.mil

ABSTRACT

Homoepitaxial Si-doped (010) β-Ga_2O_3 epitaxial layers with thicknesses ranging from 1.2 to 12 μm were grown simultaneously via close-injection showerhead metal-organic chemical vapor deposition on both Czochralski and edge-defined, film-fed grown (010) β-Ga_2O_3:Fe substrates. Structural characterization was performed via x-ray diffraction [full-width at half maxima of 21–72 arcsec depending on epilayer thickness and substrate, measured from the symmetric (020) reflection], x-ray topography, Raman spectroscopy, cathodoluminescence spectroscopy, and transmission electron microscopy. Surface characterization was performed via atomic force microscope (AFM) and Nomarski imaging, and electrical characterization was performed via electron paramagnetic resonance spectroscopy and Hall effect measurements. In addition, thermal conductivity was measured via steady-state thermoreflectance. AFM imaging revealed a number of extended defects forming in the epilayer, and transmission electron microscopy imaging detailed a V-shaped pit defect formed by misoriented twin defects likely originating from a defect at or near the substrate surface. The Hall effect data (N_S = 2.81–3.1 × 10^{17} cm^{-3} and μ_H = 81.5–103.5 cm^2/V s), surface roughness (1.78–4.25 nm rms), and thermal conductivity measurements (19.3–19.8 W/m K) yielded comparable results among all samples, independent of epilayer thickness. These results suggested that even thicker, high quality epitaxial (010) β-Ga_2O_3 could be grown via this technique, provided that the development of the observed extended defects can be mitigated.

INTRODUCTION

The high critical field ($E_C \cong 6$–8 MV/cm) of β-Ga_2O_3 suggests that high voltage vertical electronic devices can be achieved with a thinner epitaxial layer, resulting in lower specific on-resistance, faster transit times, lower switching and conduction losses, and thus higher overall circuit efficiency. Among the six phases of gallium oxide (α, β, γ, δ, ε, and κ), all of which are of scientific interest in this rapidly expanding field of research, the monoclinic (β-phase) is the only wide or ultra-wide bandgap (E_G = 4.6–4.9 eV) semiconductor platform with a large-area, melt-grown native substrate technology platform and the ability to grow thick (>10–20 μm) homoepitaxial layers with high quality and controllable doping via shallow hydrogenic donors (N_D–N_A < 10^{14} cm^{-3} to >10^{20} cm^{-3}).[1–5] These properties, as well as its thermal, chemical, and radiation stability, have positioned β-Ga_2O_3 as a leading candidate semiconductor for next-generation power devices with ultrahigh power Baliga's figure of merit in the range of 2400–3444.[6–11] Commercial homoepitaxial (001) β-Ga_2O_3 for vertical device applications is typically grown via halide vapor phase epitaxy (HVPE).[12] HVPE is the leading technique for the growth of very thick GaN drift layers; however, other epitaxial methods such as metal-organic vapor phase epitaxy (MOVPE, a.k.a., metal-organic chemical vapor deposition or MOCVD) have also been commercialized with high quality and high wafer throughput capability. Recently, high growth rate close-injection showerhead metal-organic chemical vapor deposition (CIS-MOCVD) has been developed commercially to demonstrate high quality (010) β-Ga_2O_3 epitaxial layers with electron mobilities of nearly 200 cm^2/V s at room temperature (>23 000 cm^2/V s at cryogenic temperatures) and background compensation levels of 2 × 10^{13} cm^{-3}.[13,14] The Close Injection Showerhead (CIS) design in this reactor had a 10 mm showerhead-to-susceptor gap. It features separate injection zones for oxygen and metal-organic (MO) precursors, minimizing premature oxidation and enabling faster growth rates for β-Ga_2O_3. This configuration also suppresses parasitic pre-reactions and droplet formation, improving crystalline quality and transport properties. Even though a high growth rate has been demonstrated by the CIS-MOCVD technique, device demonstrations such as lateral transistors and vertical diodes have utilized relatively thin epilayers (1–2 μm) grown at a relatively low rate of about 1–1.5 μm per hour.[15] Most recently, over 6 μm thick drift layers have been demonstrated as well.[16]

In this work, homoepitaxial (010) β-Ga_2O_3 with a thickness of up to 12 μm was grown via the CIS-MOCVD technique, and extensive characterization of these films was performed to evaluate their suitability for future β-Ga_2O_3 high voltage device development. We report film quality evaluation via several methods described below, some of which have not been applied to (010) β-Ga_2O_3 homoepitaxial layer characterization before, such as steady-state thermoreflectance (SSTR). Typically, extended defect characterization in β-Ga_2O_3 wafers is performed via the etch pit method using hot phosphoric acid.[17] It is well-known that the presence of defects such as nanopipes, particularly in (010)-oriented β-Ga_2O_3, can lead to extended defect formation in epitaxial β-Ga_2O_3. This was initially observed experimentally in vertical Schottky diodes with anode area dependence of the reverse-bias breakdown voltage.[18] Subsequently, extended defect studies, primarily via x-ray topography (XRT) techniques, have demonstrated the presence of many types of extended defects in β-Ga_2O_3 crystals and epitaxial layers.[19–31] The observed types of extended defects included stacking faults, slip planes, and threading dislocations. Cooke *et al.* have reported extended defects in ~1 μm thick MOCVD β-Ga_2O_3, showing inverted-pyramid shaped extended defects originating from underlying defects in the substrate.[31] Similar defects were observable via atomic force microscopy (AFM) imaging near the edge of similar samples of about 1 μm thick CIS-MOCVD β-Ga_2O_3 reported in the past.[15] In this work, we show the evolution of similar extended defects as a function of film thickness. With equal importance, we demonstrate that, aside from the presence of these and other defects that we have not fully understood at this time, the quality of the epitaxial films was similar in most cases, with only the thickest layers in some cases exhibiting lower mobility as well as higher rocking curve widths.

EXPERIMENTAL

Four growths were performed at Agnitron Technologies Inc. via the CIS-MOCVD technique using nominally on-axis (010) β-Ga_2O_3:Fe substrates. For each growth, a 10 × 15 mm^2 (010) edge-defined film-fed growth (EFG) and a 25 mm (1-in.) diameter (010) Czochralski-grown (CZ) wafer were co-loaded into the MOCVD reactor after a 30-min soak in concentrated hydrofluoric acid to remove silica particulates from the chemical–mechanical polishing process.[17,32,33] Epilayers of 1.2, 3.6, 6, and 12 μm thickness were successively grown at a pressure of 15 Torr, a substrate temperature of 840 °C, and a O_2/TMGa precursor flow rate ratio of 1500, with a target Si doping level of 2 × 10^{17} cm^{-3} employing silane gas and a nominal growth rate of about 1.5 μm/h. For Si doping, 25 ppm silane diluted in nitrogen (SiH_4/N_2) with a molar flow rate of 3.7 × 10^{-9} mol/min was used. During film growth, the temperature was first ramped to 700 °C, at which point gallium was introduced into the reactor to initiate deposition. A thin (~50 nm) undoped Ga_2O_3 nucleation layer was grown as the temperature increased to 750 °C. Gallium flow was then halted, and the substrate temperature was further ramped to 840 °C for the growth of the main layer.

Epitaxial layer structural characterization was performed using a modified Bruker/Jordan Valley high-resolution x-ray diffraction (HR-XRD) instrument in triple axis mode (analyzer crystal between sample and detector) with Cu $K\alpha_1$ radiation. Additional structural characterization was performed via double crystal XRT (1-BM at APS, Argonne National Laboratory), transmission electron microscopy (TEM), selected area electron diffraction (SAED) (also at Argonne National Laboratory), and the orientation map using a Tescan Tensor electron microscope.

Thermal conductivity measurements were performed via the steady-state thermoreflectance in fiber optics (SSTR-F) technique using a LaserThermal SSTR-F instrument with a 7.5 μm laser spot size.[34] Penetration depth is defined by the spot size, which makes the SSTR-F technique suitable for thermal conductivity characterization of relatively thick epitaxial layers. An 80 nm thick Al transducer layer was deposited on the β-Ga_2O_3 samples by electron beam evaporation prior to SSTR-F characterization. Areas with large-area defects on the samples were avoided in the SSTR-F instrument via software calibration before each measurement.

Polarized Raman spectroscopy was performed via a single-mode 488 nm laser beam made coaxial with the detection axis

using the beam splitter part of a volume-Bragg-grating filter set from OptiGrate. These filters allow Stokes and anti-Stokes Raman measurements closer than 10 cm^{-1} to the laser. A 50× microscope objective (NA = 0.75) was used to both focus the incident light into a small spot (~0.4 μm) and collect the scattered light, which was then dispersed in a half-meter Acton SP-2500 single-spectrometer and detected using a Princeton Instruments CCD array (Spec-10:400BR back-thinned, deep-depleted).

The electron paramagnetic resonance (EPR) measurements were done at 300 K with a commercial (E-300) Bruker Biospin 9.5 GHz spectrometer. Estimates of the spin concentrations were made from double numerical integration of fits to the EPR line shapes and the use of a well-calibrated P-doped Si standard.

AFM imaging was performed using a Bruker Dimension FastScan AFM system in tapping mode. Preliminary cathodoluminescence (CL) spectra were collected with an electron beam current of 3 μA and a beam energy of 3 keV in ultrahigh vacuum at 5 K with a 10 s integration time. Hall effect measurements were performed at room temperature using Ti/Au Ohmic contacts deposited on the corners of 5 × 5 mm sized samples and rapid-thermal annealed at 470 °C for 60 s in a N_2 atmosphere.

RESULTS AND DISCUSSION

Table I summarizes the measured rms surface roughness from AFM imaging, Hall effect measurements (carrier concentration and mobility), and thermal conductivity measured via the SSTR-F technique for each epilayer thickness. Bhattacharyya *et al.* have reported rms roughness and Hall mobility from similarly grown but lower-doped MOCVD epilayers.[16] For a 6 μm thick epilayer, the reported rms roughness values were 0.8 and 1.3 nm for 1.2 and 6.3 μm thick epilayers, respectively. Electron concentration (N_S) and Hall mobility (μ_H) values measured by the Hall technique yielded similar values for the different thickness epilayers, N_S = 2.81–3.1 × 10^{17} cm^{-3} and μ_H = 81.5–103.5 cm^2/V s, in good agreement with reported Hall mobility values for similar doping levels.[35] These were further corroborated by EPR and thermal conductivity measurements, which we have employed for additional characterization of the epitaxial layers in this study.

SSTR-F measurements were performed in a sequential automated fashion on all samples, avoiding large-area defects as a part of the calibration sequence for each sample. A consistent signal response was measured among the four samples measured via this technique, as shown in Fig. S1, confirming the measured thermal conductivity with a low degree of measurement uncertainty, as shown in Table I. This measurement, combined with the rest of the values listed in Table I, suggests that aside from the presence of large-area extended defects, the thermal conductivity of the β-Ga_2O_3 epilayers was not affected by epilayer thickness.

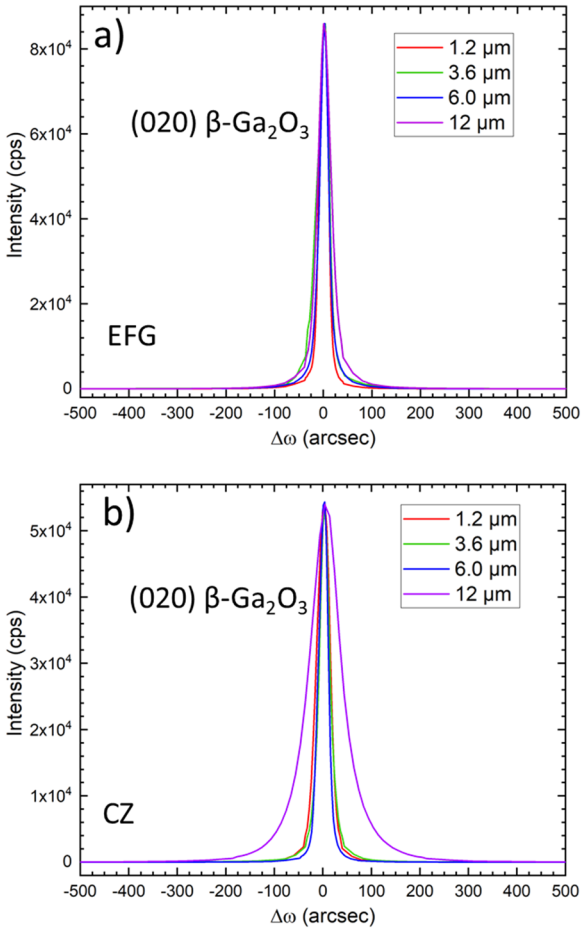

FIG. 1. X-ray diffraction on-axis omega (rocking curve) scans around the (020) reflection as a function of epilayer thickness and (a) EFG and (b) Czochralski (010) β-Ga_2O_3 substrates used for MOCVD growth.

The triple axis x-ray diffraction measurements for the CZ-based samples are shown in Figs. 1 and 2, and the full-width at half maxima (FWHM) values extracted from the omega-scans (rocking curves)

TABLE I. Summary of AFM, Hall effect, and steady-state thermoreflectance (SSTR) results from the CIS-MOCVD epitaxial β-Ga_2O_3 samples.

MOCVD epilayer thickness (μm)	Roughness, rms (nm)	Hall mobility, μ_H (cm^2/V s)	Carrier concentration, N_S (× 10^{17} cm^{-3})	Epilayer thermal conductivity (W/m K)
1.2	1.78 (10 × 10 μm)	95.5	2.9	19.8 ± 0.8
3.6	3.00 (20 × 20 μm)	103.5	2.81	19.4 ± 0.8
6.0	2.75 (20 × 20 μm)	100	2.79	19.3 ± 0.8
12	4.25 (20 × 20 μm)	81.5	3.1	19.4 ± 1.1

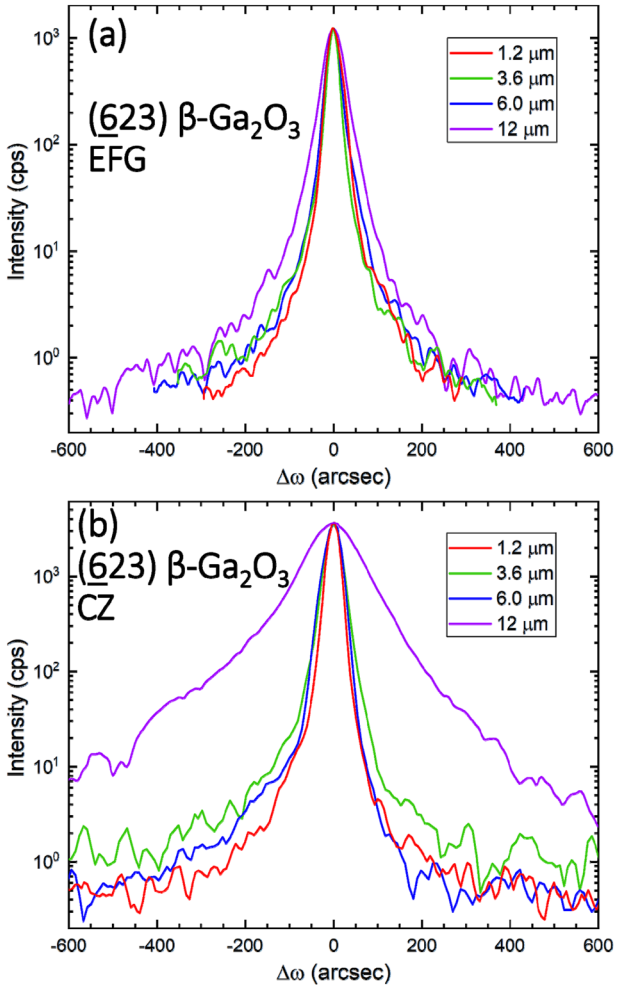

FIG. 2. Glancing exit x-ray diffraction rocking curve data aligned to the (−623) reflection with a log intensity y-axis as a function of epilayer thickness and (a) EFG and (b) Czochralski (010) β-Ga_2O_3 substrates used for MOCVD growth.

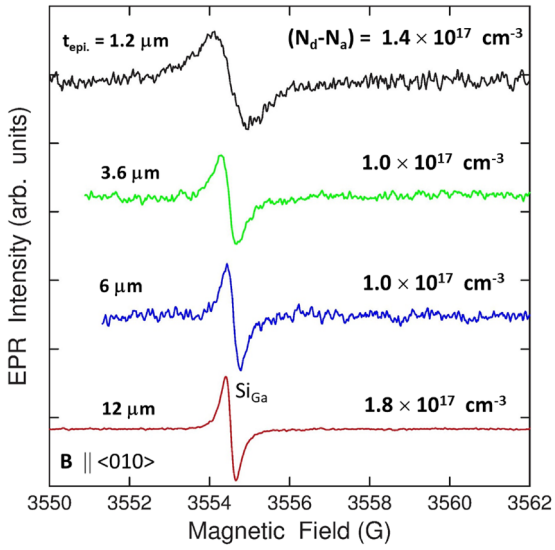

FIG. 3. EPR spectra obtained at 300 K for four Si-doped Ga_2O_3 epilayer samples grown on CZ (010) β-Ga_2O_3 substrate with varying thickness for the magnetic field (**B**) oriented parallel to the b-axis. Microwave frequency = 9.78 GHz. The spectra are displaced vertically for clarity.

around the (020) and (−623) reflections from all samples are presented in Table II. The asymmetric (−623) reflections were generated in the glancing exit (GE) geometry. The (−623) reflection was chosen to provide a more surface sensitive measurement. In this case, 95% of the diffracted intensity is from the top 1.6 μm of material. Therefore, the majority—or all—of the diffracted intensity is coming from the epitaxial layers for all of these samples. Any increased width, therefore, is not directly associated with diffraction from the substrate but rather from defects that form in the epitaxial layer or from the replication of defects that originate in the substrate. With the assumption that the substrate defects are similar for all layer thicknesses, one may conclude that any change in peak width is associated with defects that are present in the epitaxial layer. In addition, Fig. S9 of the supplementary material shows representative GE reciprocal space maps from the 6 and 12 μm samples grown on a CZ substrate.

The rocking curve full width at half maximum (FWHM) for the combined epitaxial layer and substrate for nearly all of the layers was in the range of 20–30 arcsec for the (020) reflection for all samples except the 12 μm-thick layer on the CZ substrate (74 arcsec). While XRD characterization was not possible to perform on these substrates prior to growth, separate XRD measurement of Fe-doped EFG (010) β-Ga_2O_3 bare substrate yielded a FWHM of ~20 arcsec and a FW(0.01)M of ~70 arcsec for the (020) symmetric reflection. FWHM values from the (020) reflection from EFG and CZ (010) β-Ga_2O_3 substrates have been reported by Liao *et al.* (UID EFG,

TABLE II. Summary of XRD and GEXRD data from the (020) and the (−623) reflections, respectively, from the CIS-MOCVD epitaxial β-Ga_2O_3 samples.

MOCVD epilayer thickness (μm)	(010) EFG sub. Δω (020) FWHM (arcsec)	(010) CZ sub. Δω (020) FWHM (arcsec)	(010) EFG sub. Δω (6̄23) FWHM (arcsec)	(010) CZ sub. Δω (6̄23) FWHM (arcsec)
1.2	22	32	27	27
3.6	30	25	18	33
6.0	21	24	26	32
12	32	74	42	105

13 ± 2 arcsec), Yao *et al.* (UID EFG, 28-31 arcsec), Golz *et al.* [43.2 and 104.4 arcsec for UID and Sn-doped EFG Ga_2O_3, respectively, in addition to data for many samples of (100) CZ Ga_2O_3], and Lavelle *et al.* [<50 arcsec for (010) CZ, Fe-doped].[22,36–38] The (−623) rocking curve widths were similar for most samples and are in the range of 20–30 arcsec, but the widths for the 12 μm layer thicknesses were higher—FWHM was 42 arcsec for growth on the EFG substrate and 105 arcsec for growth on the CZ substrate. In all cases, the uncertainty was less than ±1 arcsec. The larger FWHM values for the 12 μm-thick layers compared to the others correlate with the density and size of the surface defects that are present; this correlation indicates that the lattice planes in the 12 μm-thick layers are more distorted than for the other layers because of the extended defects, which will be discussed in more detail.

Hall effect measurements performed on square-sized Van der Pauw geometry samples can be affected by as much as a 20% error caused by contact geometry and size relative to sample size.[39] To confirm the carrier densities measured using the Hall effect technique via an independent technique, EPR measurements were performed at room temperature. EPR spectra obtained for the four β-Ga_2O_3:Si epilayer samples ($t_{epi.}$ = 1.2–12 μm) with the magnetic field (**B**) oriented parallel to the b-axis (**B**||⟨010⟩) are shown in Fig. 3 for a narrow field scan of 12 G.[40] A single signal is found characterized by a Zeeman splitting g-value of ~1.963 with a peak-to-valley linewidth of 0.95 G for the 1.2 μm-thick epilayer sample and sharper linewidths of 0.22–0.35 G for the three thicker epilayer samples. In addition, an angular rotation study for the 12 μm thick Si-doped β-Ga_2O_3 epilayer sample (see Fig. S2) reveals a very weak anisotropy of this signal with extremal g-values of 1.9625 with **B**||⟨010⟩ and 1.9585 with **B**⊥⟨010⟩ (we note that strong EPR signals associated with Fe^{3+} on the Ga lattice sites in the intentionally Fe-doped parent β-Ga_2O_3 bulk substrates were observed from wide magnetic field scans of 7 kG). Very similar g-values have been reported previously by several groups[15,41] from EPR studies of β-Ga_2O_3 bulk substrates and are "fingerprints" for shallow donors (both Si and Sn) and delocalized (conduction) electrons. The double numerical integration of the Lorentzian EPR line shapes and comparison with a phosphorus-doped Si standard yields a concentration of uncompensated shallow donors (N_d–N_a) for the four epilayer samples between 1.0 and 1.8 × 10^{17} cm^{-3}. These values are in good agreement with the room-temperature carrier concentrations found from the Hall effect transport results (Table I), given the typical 50% uncertainty in the quantitative EPR analyses.[42] Thus, the g-values and spin concentrations found for this EPR signal strongly support its association with the n-type Si dopants in these epilayer samples.

Figure 4 shows an x-ray topography tilt map of the 6 μm thick epilayer grown on the EFG substrate. The map was generated from multiple double crystal x-ray topography images using the (820) reflection. Overall, the material exhibited a slight lattice curvature of about 80 arcsec over a diagonal length of the sample, indicating the overall high quality of the substrate and epitaxial layer. There were a few rounded features that were 2–5 × 2–5 mm^2 in area that were slightly misoriented with the average lattice curvature. The cyan arrow points to one of these regions. The round features were also observed in optical microscopy as a higher density or clusters of pits. In this XRT image, they corresponded to regions of epitaxial β-Ga_2O_3 that were slightly misoriented by 10–20 arcsec with the surrounding material. The white arrow corresponded to a macroscopic cluster of pits over a region that was misoriented by more than the 200 arcsec range measured over the remainder of the wafer. However, from the measurements, it was not known if that region was a (010) grain that was misoriented by more than the 200 arcsec measured angular range, a different orientation, or even a polycrystalline or amorphous region.

The individual surface defect density increased with film thickness, as shown in Figs. 5 and 6. The AFM measurements in Fig. 5 were used to examine surface defects and surface roughness. Because the defect sizes were comparable in extent to the AFM scan regions, including such defects in roughness measurements would make the roughness dependent on specific locations, so the rms roughness

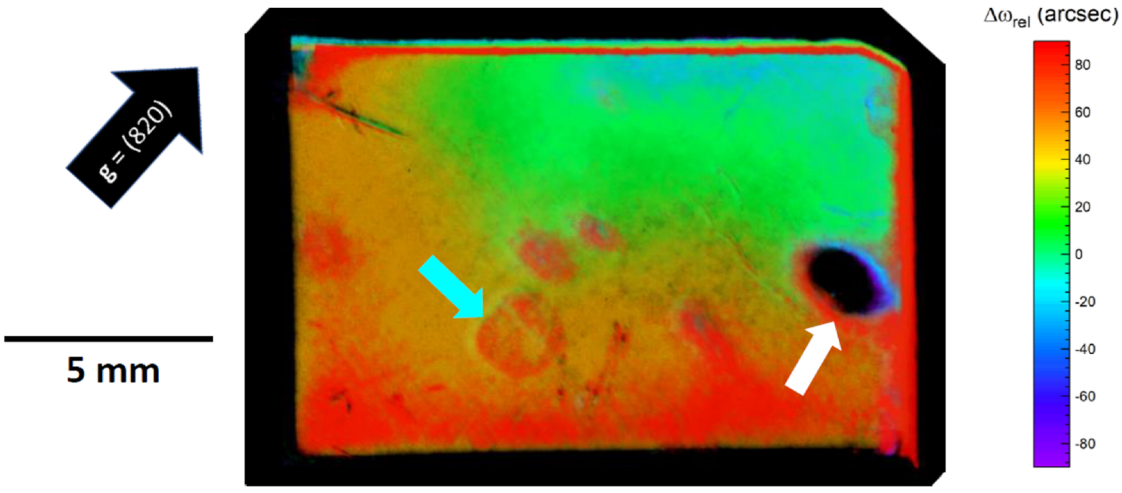

FIG. 4. Tilt map generated using x-ray topography for the 6 μm thick epilayer on EFG substrate. The defect dense region, shown as the black spot on the right side of the sample, is tilted >200° away from the rest of the material. See Figs. S10–S12 in the supplementary material for additional TEM images from this sample.

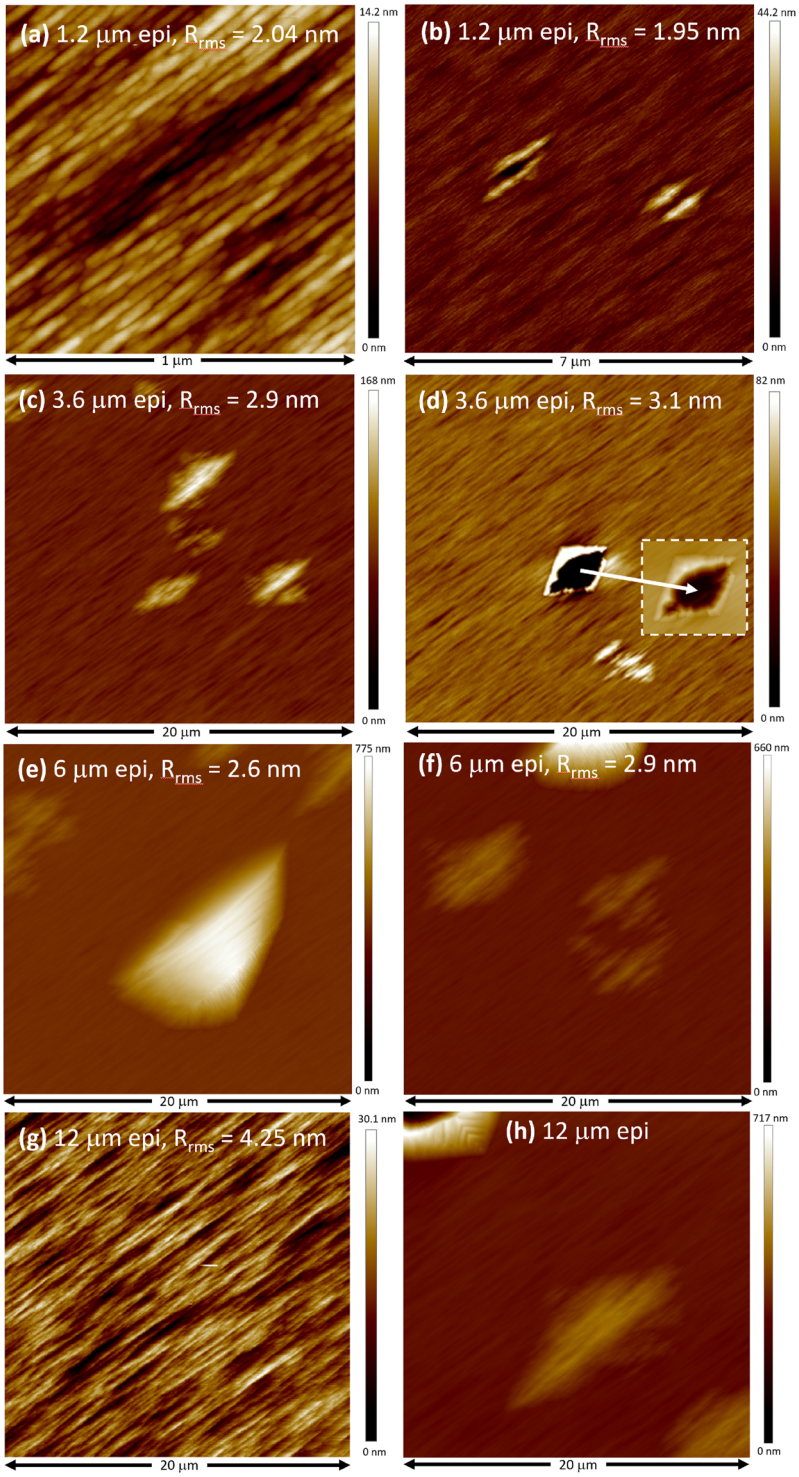

FIG. 5. AFM images of four (010) epitaxial growths on Czochralski (010) β-Ga_2O_3 substrates: (a) and (b) 1.2 μm, (c) and (d) 3.6 μm, (e) and (f) 6 μm, and (g) and (h) 12 μm. The root-mean-square roughness R_{rms} measured away from defective regions within these images is shown in Table I. Surface striations, shown in fine detail in (a), and the hillocks in (c) and (h) are oriented along the [001] direction, which is also the direction the (100) easy cleave plane intersects the (010) growth plane. As shown in (d), some defects grow into pits surrounded by parallelogram-shaped ridges; the acute-angle-corners of these parallelograms point in the direction of the surface striations. These parallelogram-shaped defects are more commonly seen with flakes growing off one or both of their obtuse-angle-corner sides.

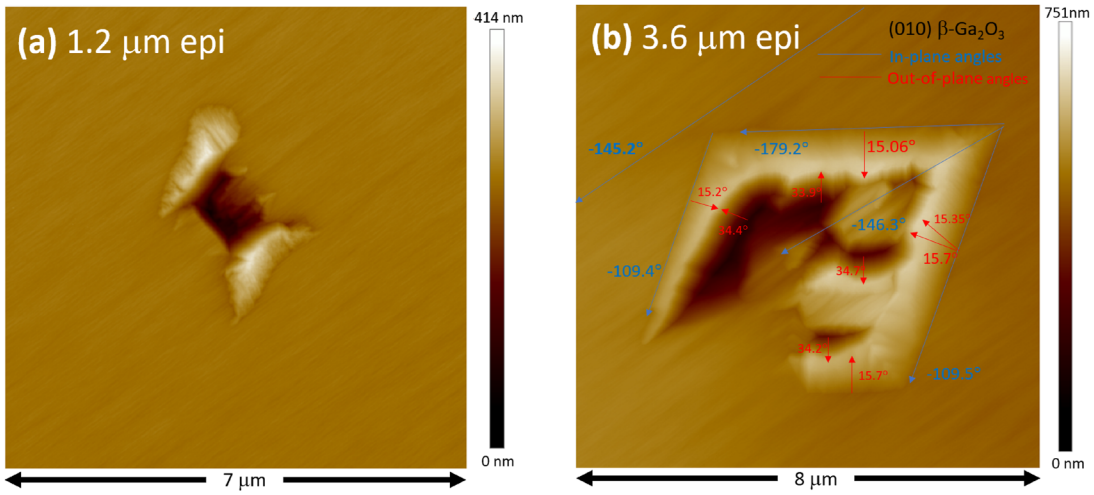

FIG. 6. AFM of defect evolution as a function of epi thickness for the (a) 1.2 μm and (b) 3.6 μm thick Ga_2O_3 epilayers on a Czochralski (010) β-Ga_2O_3 substrates.

values reported in Table I were measured in the defect-free regions. AFM images show [001] surface striations in regions apparently free of surface defects. Various types of defects are shown in the 1.2 μm epi-layer [Figs. 5(a) and 5(b)], the 3.6 μm epi-layer [Figs. 5(c) and 5(d)], the 6 μm epi-layer [Figs. 5(e) and 5(f)], and the 12 μm epi-layer [Figs. 5(g) and 5(h)]. Earlier and later growth stages of all of these various types of defects show up in different locations in the thinner and thicker epi-layers.

Figures 5(a) and 5(b) were measured on the 1.2 μm epi film. Figure 5(a) shows a closeup AFM image of the fine surface striations observed along the [001] crystalline direction in this and apparently all defect-free regions of these samples. Figure 5(b) shows a larger scan region that also contains several representative defects, which by no means exhaust the types seen. Figures 5(c) and 5(d) were measured on the 3.6 μm epi film; Fig. 5(c) shows representative "ridge" features that also have surface striations in the [001] direction; Fig. 5(d) shows a pit surrounded by a parallelogram-shaped feature whose two acute-angled-corners point along the surface striations; often such features have surface flakes growing off one or both of their obtuse-angle-corner sides. Figures 5(e) and 5(f) were measured on the 6 μm epi film; Fig. 5(e) shows a defect upon which material having surface striations along a different direction was growing; Fig. 5(f) shows a similar feature over which that growth appears to have progressed across the whole defect. Figures 5(g) and 5(h) were measured on the 12 μm epi film; Fig. 5(g) covers a seemingly defect free region, whereas Fig. 5(h) shows a ridge and the

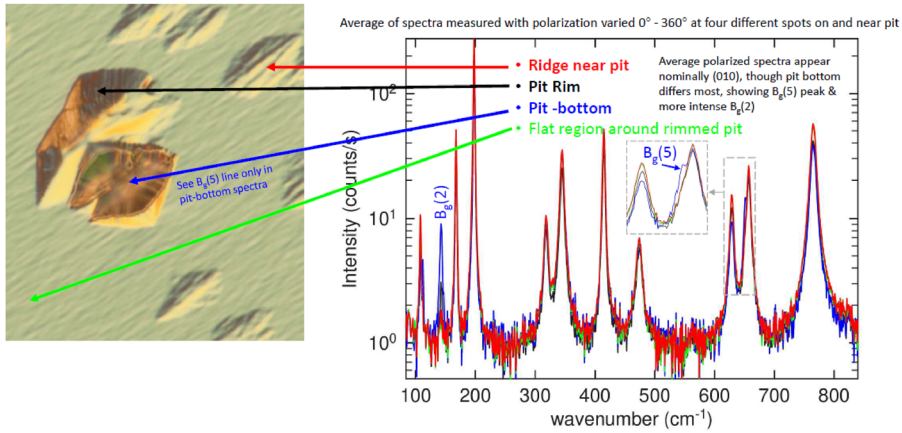

FIG. 7. Polarization-averaged z(yy)$\bar{z}$ Raman spectra for normally incident 488 nm light are plotted for the indicated spots on a 12 μm-thick (010) β-Ga_2O_3 homo-epitaxial growth on Czochralski (010) β-Ga_2O_3 substrate. Green: flat region having striations along the [001] direction. Red: ridge having striations along the [001] direction. Black: growth flake adjacent to a parallelogram shaped ridge around a pit. Blue: non-flat pit bottom. The polarization-averaged spectra for the flat (green) and ridge (red) regions, identical within the noise, correspond to (010) β-Ga_2O_3, as do the polarization-curves for the individual Raman lines (Figs. S4–S6 of the supplementary material).

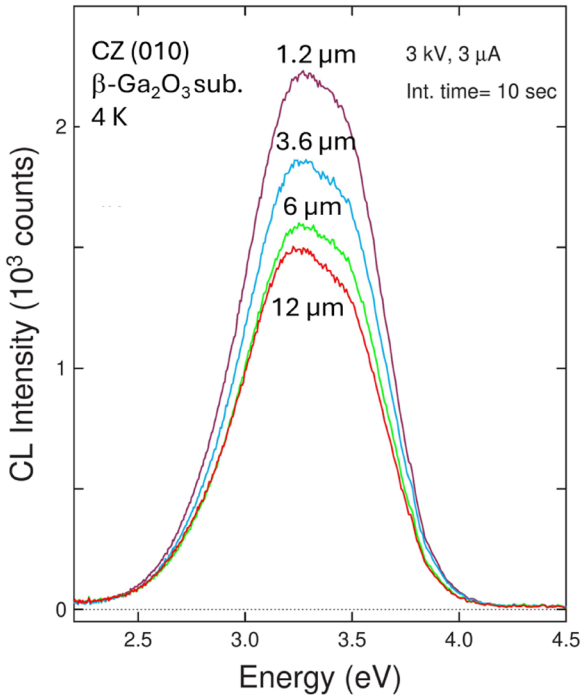

FIG. 8. Low-temperature (4 K) cathodoluminescence spectra from four samples of CIS-MOCVD β-Ga_2O_3 homoepitaxial layers grown on CZ (010) β-Ga_2O_3 substrates. All spectra were acquired from regions of the samples free from extended defects.

corner of a pit lined with a parallelogram shaped boundary. Overall, surface defects continue to nucleate, develop, and grow with increasing film thickness.

Figure 6 shows a further example of defect evolution as a function of β-Ga_2O_3 epitaxial layer thickness. The AFM images for the 1.2 μm [Fig. 6(a)] and 3.6 μm [Fig. 6(b)] thick epilayers depict the formation of the pit/parallelogram/flake defects seen in these samples. What appear to be earlier stages in Fig. 6(a) show only one feature sticking up above the normal epi surface and no pit; once such features reach a certain size, a fracture line appears on the adjacent epi-surface, which travels a short distance before being terminated by a nominally symmetric feature sticking up above the epi surface. The fracture typically enlarges to a pit around which a parallelogram feature often grows, as shown in Fig. 6(b); such parallelograms appear symmetrically oriented relative to the [001] direction of the surface striations. More commonly, large flakes begin growing at the upper-left and/or lower-right of features, as shown in Fig. 6(b). See Figs. S7 and S8 of the supplementary material for an example. The Nomarski microscope images in Fig. S8 give additional large-area illustrations of the scope of the macroscopic defects characterized in this work.

Polarized Raman spectra from various regions of the 12 μm thick β-Ga_2O_3 epilayer are shown in Fig. 7. The reader is referred to the supplementary material (Figs. S4–S6) for the detailed assignments of each Raman mode in β-Ga_2O_3.[43] These polarization averaged spectra were collected from four different spots (defect-free area, ridge, pit rim, and pit bottom), as shown in the corresponding Nomarski microscope image, confirming the phase purity of the epitaxial layers away from and within a macroscopic defect. We note

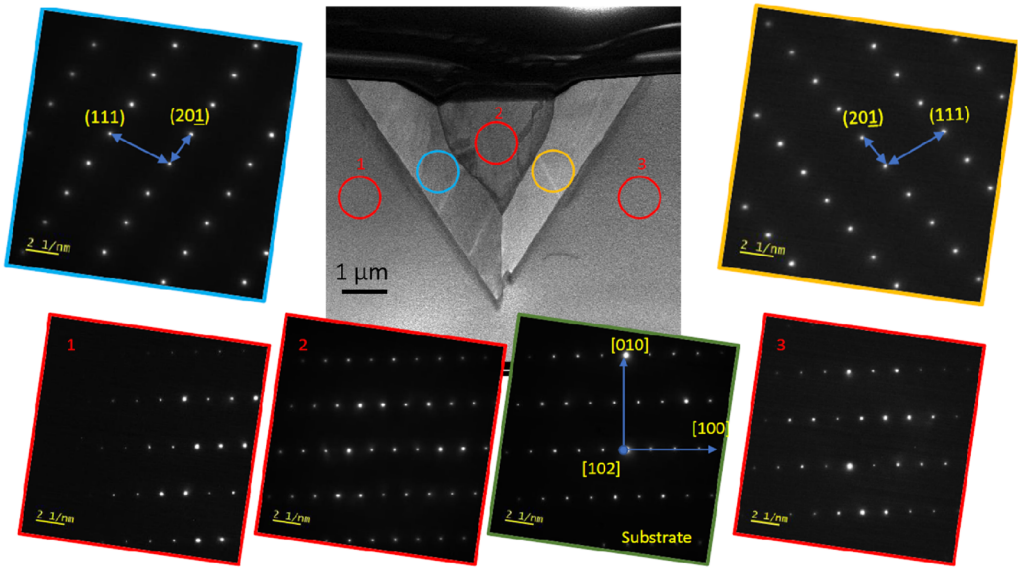

FIG. 9. Cross-sectional transmission electron micrographs and selective-area electron diffraction (SAED) images of a single V-shaped defect imaged on the 6 μm thick Ga_2O_3 epilayer on EFG (010) β-Ga_2O_3 substrate with the corresponding selected area diffraction patterns showing the presence of misoriented twin domains surrounded by bulk single crystal material. Regions 1, 2, and 3 correspond to the (010) bulk Ga_2O_3 with the [10-2] zone axis. The diffraction pattern in the green frame is a simulated pattern of (010) orientation along the [10-2] zone axis. The diffraction patterns in the yellow and blue frames are the diffraction patterns from the V-shaped components and are mirror images.

the shoulder on the $B_g(5)$ modes on the spectrum collected from a pit bottom, the origin of which is presently unknown. Further spatial maps of the intensities of the $A_g(3)$ and $A_g(10)$ modes are given in Fig. S6 of the supplementary material as a function of incident light polarization angles. The reader is further directed to Figs. S4–S6 of the supplementary material for additional angle-averaged spectra and polarization curves collected from the 12 μm thick β-Ga_2O_3 epilayer away from defects (Fig. S4), on a surface ridge (Fig. S5), and on a pit ridge (Fig. S6).

CL spectra obtained at 4 K for the β-Ga_2O_3 homoepitaxial films on Czochralski substrates are shown in Fig. 8. Monte Carlo simulation of the depth dependence of electron–hole excitation for an accelerating voltage of 3 kV yielded an estimated Bohr–Beth maximum range of 80 nm. Therefore, the CL spectra were acquired near the sample surfaces. Self-absorption was not taken into consideration because β-Ga_2O_3 is an indirect gap semiconductor and the energies of the emission bands are below the bandgap. There was a systematic reduction of the broad emission intensities with increasing film thickness, but no large variations of the emission band line shapes were observed. However, normalized peak intensity spectra (not shown) indicate a 10–15 meV rigid redshift of the CL spectrum for the 12 μm thick film and a reduction of the peak intensity around 3.40 eV. These observations may result from increasing concentration of gross structural defects across the surface of thicker films, but a direct correlation with these defects will require detailed, higher lateral resolution CL measurements.

To understand the nature of these observed defects, cross-sectional transmission electron microscopy (TEM) was taken across a single defect (Figs. 9 and 10) as well as within the high defect density region (Figs. S10–S12) (identified as the misoriented region in Fig. 4 topograph). Both TEM samples were taken along the [102] zone axis. In Fig. 9, the cross section taken across the single pit revealed a V-shaped defect with misoriented twinned grains that create a 68° angle, which corresponds to the angle with the (830) and (−830) twinned planes. This defect structure is quantifiably different from the V-shaped (a.k.a., sympetalous) defect reported in the study by Cooke *et al.*, where an 89° angle and differently oriented twinned sections were reported.[31] In addition, selected area electron diffraction measurements showed that the region between the V-shaped twinned grains exhibited the same orientation as the bulk material, suggesting a directional growth of the misoriented defect. In the defect dense region (Fig. S10), polycrystalline material was observed with elongated grains in the out-of-plane direction. Therefore, the misoriented section of material observed in the topography image was not associated with a misoriented single crystal or an amorphous region. The observed structure is reminiscent of polycrystalline growth, such as with diamond, for example, where small, nucleated grains compete during growth and eventually intersect, leaving a limited number of larger width columnar grains with a few dominant growth directions (see Fig. S10).[44] A precession electron diffraction measurement shown in Fig. S11 mapped the interfacial region, and the orientation distributions were determined. Interestingly, very little of the material was of (010), but rather a mix of orientations, with the (001) orientation the most prevalent orientation. In this defect dense region, the epilayer-substrate interface had a roughness of ~18 nm (see Fig. S12) and showed no evidence for a high quantity of threading dislocations originating from the substrate, eliminating such defects as sources for the polycrystalline growth. Overall, the high defect density in the epitaxial layers does not correspond to a high defect density in the substrates. This suggests that these V-shaped defects can also originate from surface damage (i.e., surface cleaning or polishing) and are not only associated with threading dislocations formed during bulk growth.

Figure 10 shows a proposed model for V-shaped defect formation and evolution based on the available data in this work. Figure 10(a) shows the area where the TEM lamella of width W was lifted out via the standard focused-ion beam technique. This TEM sample, shown in cross section in Fig. 10(b) (also in Fig. 9), is also shown schematically in cross-sectional side-view [Fig. 10(c)] and front-view [Fig. 10(d)]. Regions 1, 2, 3, and the substrate possess the same orientation in Fig. 10(d), suggesting that the V-shaped defect evolved at an angle with respect to the overall growth direction and the TEM images only captured one cross section. Our present hypothesis is that an imperfection at the substrate surface (e.g., a roughness or a pit) could have provided a nucleation site for the misoriented twin domains denoted with red, blue, and yellow circles in Figs. 9 and 10. Therefore, the substrate/epilayer interface imaged in Fig. 11 directly underneath the V-shaped defect would be smooth, as the substrate surface defect would not be located in the TEM sample. However, Ref. 31 did image a threading dislocation at the epilayer–substrate interface that nucleated into the V-shaped pits observed at the surface.[31]

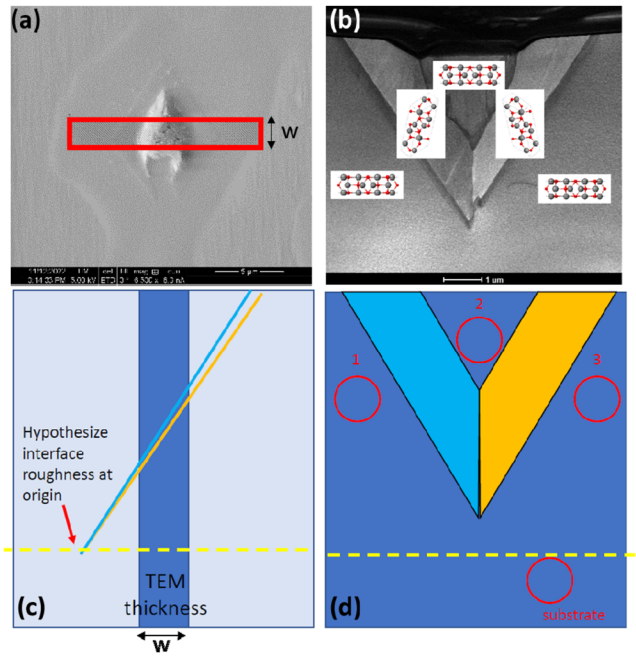

FIG. 10. Proposed model for V-shaped defect formation and evolution. (a) Scanning electron microscope (SEM) top-view image of a region with a single V-shaped defect. (b) TEM cross-sectional image from Fig. 9 shown with the correct orientation of the Ga_2O_3 domains as related to the SAED patterns. (c) Schematic showing hypothesis for origin of V-shaped defect from epitaxial interface roughness showing the cross-section of a TEM lamella with thickness W. (d) Schematic of V-shaped defect showing regions 1, 2, and 3 aligned with each other.

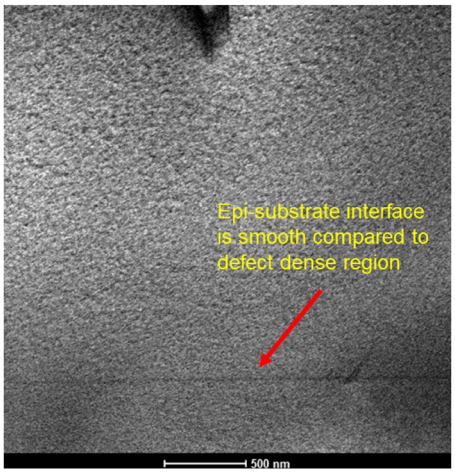

FIG. 11. Cross-sectional transmission electron micrograph of the substrate–epilayer interface underneath the V-shaped defect imaged on the 6 μm thick Ga_2O_3 epilayer on the EFG (010) β-Ga_2O_3 substrate.

CONCLUSION

The origin of surface defects was investigated in homoepitaxial (010) β-Ga_2O_3 films as a function of epilayer thickness in the 1.2–12 μm range grown via CIS-MOCVD with a substrate temperature of 840 °C and 15 Torr pressure. Optical Nomarski microscope images and AFM imaging revealed surface pitting distributed nonuniformly across the sample, with regions of high and low density of surface defects. AFM imaging profiled the evolution of extended defects as a function of epilayer thickness. Detailed polarized Raman spectroscopy analysis showed only the presence of monoclinic β-phase Ga_2O_3 within the extended defects. TEM imaging revealed a V-shaped defect consisting of misoriented twins of β-Ga_2O_3 in the 6 μm thick film. EPR spectra and Hall measurements showed good agreement in Si doping levels of 2.8–3.1 $\times 10^{17}$ cm^{-3}, with slightly lower mobilities associated with the higher defect densities that also led to broadened (020) and (−623) rocking curves. Thermal conductivity measurements performed away from the extended defects were in the range of 19.3–19.8 W/m K, also independent of epilayer thickness. These results suggest that extended defects are the primary killer defect in thick CIS-MOCVD epitaxial β-Ga_2O_3, at least for the case of growth using on-axis (010) β-Ga_2O_3 substrates. Growth of Ga_2O_3 with excellent growth rate and high structural and electrical quality has been reported in the literature via various techniques, including molecular beam epitaxy, hot-wall MOCVD, and mist-CVD techniques, as well as the close-coupled showerhead MOCVD from a different reactor manufacturer.[45–51] While the quality of epitaxial Ga_2O_3 continues to improve, at this time, the understanding and elimination of extended defects still remain priorities in order to produce epitaxial layers with relevant thickness for ultrahigh voltage power electronics applications.

SUPPLEMENTARY MATERIAL

In the supplementary material, we include the following additional data: resistance vs input power SSTR signal, EPR spectra, Raman maps, spectra, polarization curves, Nomarski and AFM images of extended defects, representative GE RSM maps, and TEM images.

ACKNOWLEDGMENTS

The authors are sincerely grateful to Dr. Michael Mastro (NRL), Dr. Jennifer Hite (NRL, presently at Univ. of Florida), and Dr. Charles (Chip) Eddy (NRL retired) for the support of CIS-MOCVD development and preliminary FIB imaging. Research at NRL was supported by the Office of Naval Research. CIS-MOCVD research and development at Agnitron was partially supported by the Office of Naval Research (Capt. Lynn Petersen) and the Air Force Office of Scientific Research (AFOSR). This research used resources of the Advanced Photon Source, a U.S. Department of Energy (DOE) Office of Science User Facility operated for the DOE Office of Science by Argonne National Laboratory under Contract No. DE-AC02-06CH11357. Research at the University of Virginia was supported as part of APEX (A Center for Power Electronics Materials and Manufacturing Exploration), an Energy Frontier Research Center funded by the U.S. Department of Energy (DOE), Office of Science, Basic Energy Sciences (BES), under Award No. ERW0345. The synchrotron x-ray topography measurements were carried out at the 1-BM beamline of the Advanced Photon Source, Argonne National Laboratory. TEM sample preparation and measurements were performed at the Center for Nanoscale Materials, Argonne National Laboratory. M.L., J.S.L., and H.M. gratefully acknowledge the postdoctoral support from the National Research Council. Sample dicing was performed by Mr. Milton Rebbert (NRL retired). The authors are sincerely grateful to the Air Force Research Laboratory (John Blevins) and Novel Crystal Technology Inc. (Akito Kuramata, Kohei Sasaki) for the β-Ga_2O_3 substrate supply.

AUTHOR DECLARATIONS

Conflict of Interest

The authors have no conflicts to disclose.

Author Contributions

Marko J. Tadjer: Conceptualization (equal); Data curation (equal); Formal analysis (equal); Funding acquisition (equal); Investigation (equal); Methodology (equal); Project administration (equal); Supervision (equal); Writing – original draft (equal); Writing – review & editing (equal). **Kenny Hyunh**: Data curation (equal); Formal analysis (equal); Investigation (equal); Methodology (equal). **James C. Culbertson**: Data curation (equal); Formal analysis (equal); Investigation (equal); Methodology (equal); Writing – review & editing (equal). **Evan R. Glaser**: Data curation (equal); Formal analysis (equal); Investigation (equal); Methodology (equal); Writing – review & editing (equal). **Michael E. Liao**: Formal analysis (equal); Investigation (equal); Methodology (equal). **John Gaskins**: Data curation (equal); Formal analysis (equal); Investigation (equal); Methodology (equal). **Hannah N. Masten**: Data curation (equal); Formal analysis (equal); Investigation (equal); Methodology (equal). **Alan G. Jacobs**: Formal analysis (equal); Investigation (equal); Methodology (equal). **Nadeem A. Mahadik**: Data curation (equal); Formal analysis (equal); Investigation (equal); Methodology (equal). **James Spencer Lundh**: Data curation (equal);

Formal analysis (equal); Investigation (equal); Methodology (equal). **Jaime A. Freitas, Jr.**: Data curation (equal); Formal analysis (equal); Investigation (equal); Methodology (equal). **Fikadu Alema**: Conceptualization (equal); Funding acquisition (equal); Investigation (equal); Methodology (equal); Supervision (equal). **Andrei Osinsky**: Conceptualization (equal); Funding acquisition (equal); Methodology (equal); Project administration (equal); Resources (equal). **Patrick Hopkins**: Data curation (equal); Formal analysis (equal); Investigation (equal); Methodology (equal); Resources (equal); Supervision (equal). **Mark Goorsky**: Data curation (equal); Formal analysis (equal); Investigation (equal); Methodology (equal); Resources (equal); Supervision (equal); Validation (equal); Writing – review & editing (equal). **Karl D. Hobart**: Conceptualization (equal); Funding acquisition (equal); Project administration (equal); Resources (equal); Supervision (equal).

DATA AVAILABILITY

The data that support the findings of this study are available from the corresponding author upon reasonable request.

REFERENCES

[1] M. J. Tadjer, J. L. Lyons, N. Nepal, J. A. Freitas, A. D. Koehler, and G. M. Foster, "Review—Theory and characterization of doping and defects in β-Ga_2O_3," ECS J. Solid State Sci. Technol. **8**(7), Q3187–Q3194 (2019).

[2] V. Gottschalch, S. Merker, S. Blaurock, M. Kneiß, U. Teschner, M. Grundmann, and H. Krautscheid, "Heteroepitaxial growth of α-β-γ-and κ-Ga_2O_3 phases by metalorganic vapor phase epitaxy," J. Cryst. Growth **510**, 76 (2019).

[3] A. Polyakov, V. Nikolaev, S. Stepanov, A. Almaev, A. Pechnikov, E. Yakimov, B. O. Kushnarev, I. Shchemerov, M. Scheglov, A. Chernykh, A. Vasilev, A. Kochkova, and S. J. Pearton, J. Appl. Phys. **131**, 215701 (2022).

[4] M. Bosi, P. Mazzolini, L. Seravalli, and R. Fornari, "Ga_2O_3 polymorphs: Tailoring the epitaxial growth conditions," J. Mater. Chem. C **8**, 10975 (2020).

[5] Y. Oshima, E. G. Víllora, and K. Shimamura, "Halide vapor phase epitaxy of twin-free α-Ga_2O_3 on sapphire (0001) substrates," Appl. Phys. Express **8**, 055501 (2015).

[6] Y. Zhang and J. S. Speck, Semicond. Sci. Technol. **35**, 125018 (2020).

[7] M. Higashiwaki, K. Sasaki, A. Kuramata, T. Masui, and S. Yamakoshi, "Gallium oxide (Ga_2O_3) metal-semiconductor field-effect transistors on single-crystal β-Ga_2O_3 (010) substrates," Appl. Phys. Lett. **100**, 013504 (2012).

[8] A. Azarov, J. G. Fernández, J. Zhao, F. Djurabekova, H. He, R. He, Ø. Prytz *et al.*, "Universal radiation tolerant semiconductor," Nat. Commun. **14**, 4855 (2023).

[9] A. I. Titov, K. V. Karabeshkin, A. I. Struchkov, V. I. Nikolaev, A. Azarov, D. S. Gogova, and P. A. Karaseov, Vacuum **200**, 111005 (2022).

[10] S. Ohira and N. Arai, Phys. Status Solidi C **5**, 3116–3118 (2008).

[11] V. G. Hill, R. Roy, and E. F. Osborn, "The system alumina-gallia-water," J. Am. Ceram. Soc. **35**, 135–142 (1952).

[12] H. Murakami, K. Nomura, K. Goto, K. Sasaki, K. Kawara, Q. T. Thieu, R. Togashi *et al.*, "Homoepitaxial growth of β-Ga_2O_3 layers by halide vapor phase epitaxy," Appl. Phys. Express **8**, 015503 (2014).

[13] G. Seryogin, F. Alema, N. Valente, H. Fu, E. Steinbrunner, A. T. Neal, S. Mou, A. Fine, and A. Osinsky, "MOCVD growth of high purity Ga_2O_3 epitaxial films using trimethylgallium precursor," Appl. Phys. Lett. **117**, 262101 (2020).

[14] L. Meng, Z. Feng, A. F. M. A. U. Bhuiyan, and H. Zhao, Cryst. Growth Des. **22**(6), 3896–3904 (2022).

[15] M. J. Tadjer, F. Alema, A. Osinsky, M. A. Mastro, N. Nepal, J. M. Woodward, R. L. Myers-Ward *et al.*, "Characterization of β-Ga_2O_3 homoepitaxial films and MOSFETs grown by MOCVD at high growth rates," J. Phys. D: Appl. Phys. **54**, 034005 (2020).

[16] A. Bhattacharyya, C. Peterson, K. Chanchaiworawit, S. Roy, Y. Liu, S. Rebollo, and S. Krishnamoorthy, "Over 6 μm thick MOCVD-grown low-background carrier density (1015 cm^{-3}) high-mobility (010) β-Ga_2O_3 drift layers," Appl. Phys. Lett. **124**, 010601 (2024).

[17] A. Kuramata, K. Koshi, S. Watanabe, Y. Yamaoka, T. Masui, and S. Yamakoshi, "High-quality β-Ga_2O_3 single crystals grown by edge-defined film-fed growth," Jpn. J. Appl. Phys. **55**, 1202A2 (2016).

[18] J. Yang, S. Ahn, F. Ren, S. J. Pearton, S. Jang, and A. Kuramata, "High breakdown voltage (−201) β-Ga_2O_3 Schottky rectifiers," IEEE Electron Device Lett. **38**, 906–909 (2017).

[19] N. A. Mahadik, M. J. Tadjer, P. L. Bonanno, K. D. Hobart, R. E. Stahlbush, T. J. Anderson, and A. Kuramata, "High-resolution dislocation imaging and microstructural analysis of HVPE-$\beta$$Ga_2O_3$ films using monochromatic synchrotron topography," APL Mater. **7**, 022513 (2019).

[20] L. Meng, A. F. M. A. U. Bhuiyan, Z. Feng, H.-L. Huang, J. Hwang, and H. Zhao, "Metalorganic chemical vapor deposition of (100) β-Ga_2O_3 on on-axis Ga_2O_3 substrates," J. Vac. Sci. Technol., A **40**, 062706 (2022).

[21] H. Yamaguchi and A. Kuramata, "Stacking faults in β-Ga_2O_3 crystals observed by X-ray topography," J. Appl. Crystallogr. **51**, 1372–1377 (2018).

[22] Y. Yao, Y. Ishikawa, and Y. Sugawara, "Slip planes in monoclinic β-Ga_2O_3 revealed from its {010} face via synchrotron X-ray diffraction and X-ray topography," Jpn. J. Appl. Phys. **59**, 125501 (2020).

[23] Y. Yao, Y. Sugawara, and Y. Ishikawa, "Identification of Burgers vectors of dislocations in monoclinic β-Ga_2O_3 via synchrotron x-ray topography," J. Appl. Phys. **127**, 205110 (2020).

[24] Y. Yao, K. Hirano, Y. Sugawara, K. Sasaki, A. Kuramata, and Y. Ishikawa, "Observation of dislocations in thick β-Ga_2O_3 single-crystal substrates using Borrmann effect synchrotron x-ray topography," APL Mater. **10**, 051101 (2022).

[25] Y. Yao, Y. Sugawara, and Y. Ishikawa, "Observation of dislocations in β-Ga_2O_3 single-crystal substrates by synchrotron X-ray topography, chemical etching, and transmission electron microscopy," Jpn. J. Appl. Phys. **59**, 045502 (2020).

[26] Y. Yao, Y. Tsusaka, K. Sasaki, A. Kuramata, Y. Sugawara, and Y. Ishikawa, "Large-area total-thickness imaging and Burgers vector analysis of dislocations in β-Ga_2O_3 using bright-field x-ray topography based on anomalous transmission," Appl. Phys. Lett. **121**, 012105 (2022).

[27] Y. Yao, Y. Tsusaka, K. Hirano, K. Sasaki, A. Kuramata, Y. Sugawara, and Y. Ishikawa, "Three-dimensional distribution and propagation of dislocations in β-Ga_2O_3 revealed by Borrmann effect x-ray topography," J. Appl. Phys. **134**, 155104 (2023).

[28] Y. Yao, Y. Ishikawa, and Y. Sugawara, "Dislocation classification of a large-area β-Ga_2O_3 single crystal via contrast analysis of affine-transformed X-ray topographs," J. Cryst. Growth **548**, 125825 (2020).

[29] M. I. Chaman, K. Hoshikawa, S. Sdoeung, and M. Kasu, "High crystal quality of vertical Bridgman and edge-defined film-fed growth β-Ga_2O_3 bulk crystals investigated using high-resolution X-ray diffraction and synchrotron X-ray topography," Jpn. J. Appl. Phys. **61**, 055501 (2022).

[30] S. Sdoeung, K. Sasaki, K. Kawasaki, J. Hirabayashi, A. Kuramata, and M. Kasu, "Characterization of dislocation of halide vapor phase epitaxial (001) β-Ga_2O_3 by ultrahigh sensitive emission microscopy and synchrotron X-ray topography and its influence on Schottky barrier diodes," Jpn. J. Appl. Phys. **62**, SF1001 (2023).

[31] J. Cooke, P. Ranga, A. Bhattacharyya, X. Cheng, Y. Wang, S. Krishnamoorthy, M. A. Scarpulla, and B. Sensale-Rodriguez, "Sympetalous defects in metalorganic vapor phase epitaxy (MOVPE)-grown homoepitaxial β-Ga_2O_3 films," J. Vac. Sci. Technol., A **41**, 013406 (2023).

[32] J. D. Blevins, K. Chabak, G. Jessen, D. Thomson, K. Stevens, G. Foundos, A. Lindsey, J. H. Leach, J. Rumsey, and A. Green, "Growth of 50 mm beta-gallium oxide (β-Ga_2O_3) substrates," in *CS Mantech Conference Prococeedings 2018* (CS Mantech, 2018), p. 013.5, https://csmantech.org/digests/.

[33] J. D. Blevins, A. Brady, G. Foundos, C. Scott, D. Snyder, W. Everson, R. Lavelle, and V. Gambin, "Manufacturing challenges of Czochralski growth and fabrication of 2-inch semi-insulating β-Ga_2O_3 substrates," in *CS Mantech Conference Prococeedings 2022* (CS Mantech, 2022) pp. 291–294, https://csmantech.org/digests/.

[34] J. L. Braun, D. H. Olson, J. T. Gaskins, and P. E. Hopkins, "A steady-state thermoreflectance method to measure thermal conductivity," Rev. Sci. Instrum. **90**, 024905 (2019).

[35]J. A. Spencer, M. J. Tadjer, A. G. Jacobs, M. A. Mastro, J. L. Lyons, J. A. Freitas, J. C. Gallagher *et al.*, "Activation of implanted Si, Ge, and Sn donors in high-resistivity halide vapor phase epitaxial β-Ga_2O_3:N with high mobility," Appl. Phys. Lett. **121**, 192102 (2022).
[36]C. Golz, Z. Galazka, J. Lähnemann, V. Hortelano, F. Hatami, W. Ted Masselink, and O. Bierwagen, "Electrical conductivity tensor of β-Ga_2O_3 analyzed by van der Pauw measurements: Inherent anisotropy, off-diagonal element, and the impact of grain boundaries," Phys. Rev. Mater. **3**, 124604 (2019).
[37]M. E. Liao, K. Huynh, L. Matto, D. P. Luccioni, and M. S. Goorsky, "Optimization of chemical mechanical polishing of (010) β-Ga_2O_3," J. Vac. Sci. Technol., A **41**, 013205 (2023).
[38]R. M. Lavelle, W. J. Everson, D. J. Erdely, L. A. M. Lyle, S. W. Pistner, S. R. Hallacher, J. M. Redwing, and D. W. Snyder, "Chemical-mechanical polishing improvements and subsurface damage elimination for Cz grown (010) β-Ga_2O_3 substrates," Mater. Sci. Semicond. Process. **190**, 109341 (2025).
[39]R. Chwang, B. J. Smith, and C. R. Crowell, "Contact size effects on the van der Pauw method for resistivity and Hall coefficient measurement," Solid-State Electron. **17**, 1217–1227 (1974).
[40]A. Venzie, M. Stavola, W. B. Fowler, E. R. Glaser, M. J. Tadjer, J. I. Forbus, M. E. Zvanut, S. J. Pearton, and S. J. Pearton, "Assignments of vibrational lines to OD-impurity complexes for adventitious impurities in β-Ga_2O_3," APL Mater. **12**, 071108 (2024).
[41]N. T. Son, K. Goto, K. Nomura, Q. T. Thieu, R. Togashi, H. Murakami, Y. Kumagai, A. Kuramata, M. Higashiwaki, A. Koukitu, S. Yamakoshi, B. Monemar, and E. Janzén, "Electronic properties of the residual donor in unintentionally doped β-Ga_2O_3," J. Appl. Phys. **120**, 235703 (2016), and references therein.
[42]See, for example S. Bhandari and M. E. Zvanut, "Optical transitions for impurities in Ga_2O_3 as determined by photo-induced electron paramagnetic resonance spectroscopy," J. Appl. Phys. **127**, 065704 (2020).
[43]C. Kranert, C. Sturm, R. Schmidt-Grund, and M. Grundmann, "Raman tensor elements of β-Ga_2O_3," Sci. Rep. **6**, 35964 (2016).
[44]O. A. Williams, "Nanocrystalline diamond," Diamond Relat. Mater. **20**, 621–640 (2011), and references therein.
[45]S.-Y. Park, M.-T. Ha, K.-H. Kim, L. Van Lich, Y.-J. Shin, S.-M. Jeong, S.-H. Kwon, and S.-Y. Bae, Ceram. Int. **48**, 5075 (2022).
[46]K. Itenaga, N. Tanaka, T. Nishimura, H. Iino, K. Goto, M. Ishikawa, H. Machida, T. Ueno, and Y. Kumagai, J. Cryst. Growth **582**, 126520 (2022).
[47]D. Gogova, M. Ghezellou, D. Q. Tran, S. Richter, A. Papamichail, J. u. Hassan, A. R. Persson, P. O. Å. Persson, O. Kordina, B. Monemar, M. Hilfiker, M. Schubert, P. P. Paskov, and V. Darakchieva, AIP Adv. **12**, 055022 (2022).
[48]D. Gogova, D. Q. Tran, V. Stanishev, V. Jokubavicius, L. Vines, M. Schubert, R. Yakimova, P. P. Paskov, and V. Darakchieva, J. Vac. Sci. Technol., A **42**, 022708 (2024).
[49]A. Waseem, G. M. Latham, C. McAleese, S. Omar, I. Sanyal, D. M. Dryden, A. Pakes, and X. Li, Appl. Phys. Rev. **12**, 021412 (2025).
[50]P. Mazzolini and O. Bierwagen, J. Phys. D: Appl. Phys. **53**, 354003 (2020).
[51]A. Mauze, Y. Zhang, T. Itoh, F. Wu, and J. S. Speck, APL Mater. **8**, 021104 (2020).